Attached Decelerating Turbulent Boundary Layers over Riblets

Benjamin S. Savino*[1], Amirreza Rouhi†[2], and Wen Wu‡[1]
1. Department of Mechanical Engineering, University of Mississippi, University, MS, 38677, USA
2. Department of Engineering, Nottingham Trent University, Nottingham, NG1 4FQ, UK

Turbulent boundary layers (TBLs) over riblets subjected to freestream adverse pressure gradients (APGs) are investigated by direct numerical simulation. The reference zero-pressure-gradient (ZPG) boundary layer is initialized at a Reynolds number of $Re_\delta = 6800$ before entering the APG region. Downstream, the TBLs then develop under the APG for 30 boundary layer thickness (δ). We examine two APG strengths (peak $\beta \approx 5$ and 10), three riblet sizes (s^+=16, 26, and 60), and corresponding smooth-wall cases. This case matrix allows us to evaluate riblet-induced drag modification and the associated physical mechanisms across drag-modulation regimes previously identified for ZPG riblet flows. The flow remains attached in all the cases. An immersed boundary method, together with fine grid resolution, is employed to resolve the flow within the riblet grooves and the TBL. The simulations show that, under APGs, riblets can reduce drag far beyond what has been achieved in ZPG flows. For large riblet sizes under strong APG, the riblets even generate an upstream force, corresponding to negative drag. The substantial drag reduction is attributed to Kelvin–Helmholtz (KH) roller vortices that form near the riblet crest. The vortices' size, strength, and wavelength are founded to be governed primarily by the local APG at their generation site. The results presented here suggest that existing drag-characterization metrics, as well as criteria for the onset of KH rollers, may require modifications when the pressure gradient is non-negligible.

I. Introduction

Riblets are among the most extensively studied passive drag-reduction techniques, and have been shown to reduce friction drag by up to 10% in canonical turbulent flows (i.e., zero-pressure-gradient (ZPG) turbulent boundary layers (TBLs) and fully developed turbulent channels) [1–15]. The fundamental shortcoming of riblet research over the past four decades, however, is that emphasis has been placed on understanding their effect in equilibrium ZPG flows. Meanwhile, in practice, they are employed to reduce drag in various aeronautical, maritime, and energy sectors. For example, Lufthansa and AeroSHARK have begun applying riblet films to commercial airliners to investigate efficiency gains on an industrial scale [16].

Turbulent flows in such complex settings, however, rarely exhibit the well-behaved characteristics of ZPG TBLs and channel flows where riblets have typically been studied. A common non-equilibrium influence present in many practical applications is the pressure gradient (PG). PGs in flows around or through complex geometries can be caused by converging or diverging surfaces, a feature far more prevalent than flat surfaces in engineering contexts. For instance, flow over the suction side of an airfoil experiences a strong, spatially evolving adverse pressure gradient (APG), which significantly alters both the turbulence structure and the mean flow characteristics [17, 18]. Moreover, temporal variations in the driving force — such as those in piping and closed-loop fluid systems, fluctuations in ambient or freestream velocity, or flow driven by reciprocating pumps — can also induce transient or sustained changes in the PG. It remains largely unknown how riblets interact with non-equilibrium, spatially developing turbulence, and whether they maintain their drag-reducing properties when the flow is dominated by significant PGs. This hinders the effective use of riblets to reduce drag in realistic flow settings. Despite this uncertainty, reduced-order turbulence models used to represent the effects of riblets in engineering flows are often developed under the assumption that their behavior in ZPG flows carries over to spatially developing, PG-dominated flows [19, 20].

The limited understanding of riblet effectiveness in non-equilibrium flows motivates the present study, in which we focus on the APG. A few investigations have explored the influence of riblets in APG TBLs, both experimentally [21–23] and computationally [24, 25]. In general, these studies have shown that drag reduction tends to increase under APG conditions — relative to ZPG cases — with reductions of up to approximately 15%. However, the underlying physical

*Ph.D. Candidate, AIAA Student Member
†Senior Lecturer
‡Assistant Professor. AIAA Senior Member. Corresponding author. Email address: wu@olemiss.edu

mechanisms responsible for this enhanced drag reduction remain largely unexplored. Moreover, these studies focus on weak APGs, characterized by Clauser parameter, $\beta = (\delta^*/\tau_w)(dP/dx)$, of order 0.1-1, with little to no spatial variation. As a result, these weak APG TBLs differ little from canonical ZPG TBLs and often retain a (weak) self-similarity of the TBL, thus enabling characterization using laws similar to ZPG ones. Therefore, the viscous-scaled peak-to-peak riblet spacing ($s^+ = su_\tau/\nu$, where u_τ is the friction velocity and ν is the kinematic viscosity), a typical metric for gauging drag modulation in ZPG flows [2, 9], does not exhibit considerable variation in many of these studies. It always remains in the drag-reducing regime ($s^+ \in [0,\ 25]$). These features are not representative of many relevant flows, which as previously noted experience significantly stronger APGs and exhibit considerable spatial development. For example, on the suction side of an airfoil, β can reach values of order 10^2 along the chord length even for an attached flow[26, 27].

The objective of this work is to investigate the influence of riblets in strong, spatially evolving APGs. The strong APG will result in significant spatial variation of u_τ, which in turn varies the viscous-scaled riblet size across the domain. This, in conjunction with testing riblets of various physical sizes, allows the examination of riblet effectiveness in various regimes based on scaling laws developed in ZPG flows. These include: drag-reducing, drag-augmenting, and Kelvin-Helmholtz (KH)-roller-inducing (further discussion is provided in Sec. II(b)). This will allow us to: 1) characterize drag modification in these various regimes during flow deceleration; 2) determine whether the quantitative metrics predicting drag reduction and increase from ZPG flows hold in APG flows; and 3) determine if the physical mechanisms responsible for drag modification in these regimes are the same in ZPG and APG flows. In the remainder of the paper, we will first summarize the configuration and numerical methods in Section II, then discuss initial findings including boundary layer development, mean and instantaneous velocity fields, preliminary turbulence statistics, and shear layer quantities in Section III.

II. Methodology

A. Problem formulation

TBLs over smooth and riblet-covered walls subjected to APGs are simulated by direct numerical simulations (DNS). The APG is induced by imposing a decelerating freestream velocity profile along the top of the computational domain ($U_\infty(x)$, where x is the streamwise direction), while the wall-normal velocity ($V_\infty(x)$) is determined by wall-normal integral mass conservation during runtime [28]. While some previous computational studies have applied a power-law distribution of $U_\infty(x)$ to achieve quasi-equilibrium decelerating boundary layers[29–31], the near-constant resultant Clauser parameter (β) is often small (typically $\leq O(1)$), indicating only a slight deviation from a conventional ZPG TBL and resulting in slow streamwise development. In the present study, a decreasing hyperbolic-tangent freestream velocity distribution is employed to induce a strong, spatially varying APG, thereby producing substantial variation in riblet spacing in wall units across the computational domain.

Two levels of deceleration are examined, as shown in figure 1. The freestream velocity is decreased by 20% and 25%, respectively, over $30\delta_o$. The resulting Clauser parameter is shown in the middle panel of the figure. Here, the displacement thickness is calculated as:

$$\delta^*(x) = \int_0^{\delta(x)} \left(1 - \frac{U(x,y)}{U_e(x)}\right) dy, \tag{1}$$

where $\delta(x)$ is the local boundary layer thickness determined using the method described by Griffin *et al.* [32], $U_e(x)$ is the mean streamwise velocity at the boundary layer edge, and y is the wall-normal direction. Over the smooth wall, the resulting peak values of β are approximately 5 and 10 (figure 1b), representing significantly stronger APGs than previously investigated for riblet-covered walls in Refs. [21–25]. The friction velocity on the smooth wall decreases by $\sim 40\%$ and $\sim 55\%$ by the end of the domain in in the two cases (figure 1c). Thus, neither APG is sufficiently strong, nor acts over sufficient distance, to separate the flow.

At the domain inlet, instantaneous velocity fields from an *a-priori* DNS of a ZPG TBL are applied. The flow is allowed to develop under ZPG (i.e., constant U_∞) for approximately 20 boundary layer thicknesses (δ) until it reaches $Re_\delta = 6800$ in all cases, after which the the decelerating U_∞ is applied. This streamwise location is hereafter referred to as the 'reference location' (i.e., $x = 0$). Quantities at the reference location are indicated with the subscript 'o'. The remaining boundary conditions are: no-slip on the bottom wall (riblet or smooth), periodic in the spanwise direction, and convective outflow.

The streamwise (L_x), wall-normal (L_y), and spanwise (L_z) computational domain sizes for each case are provided in Table 1. $L_x \approx 55\delta_o$ is chosen to 1) provide a 20δ quasi-ZPG development region upstream of the APG zone so

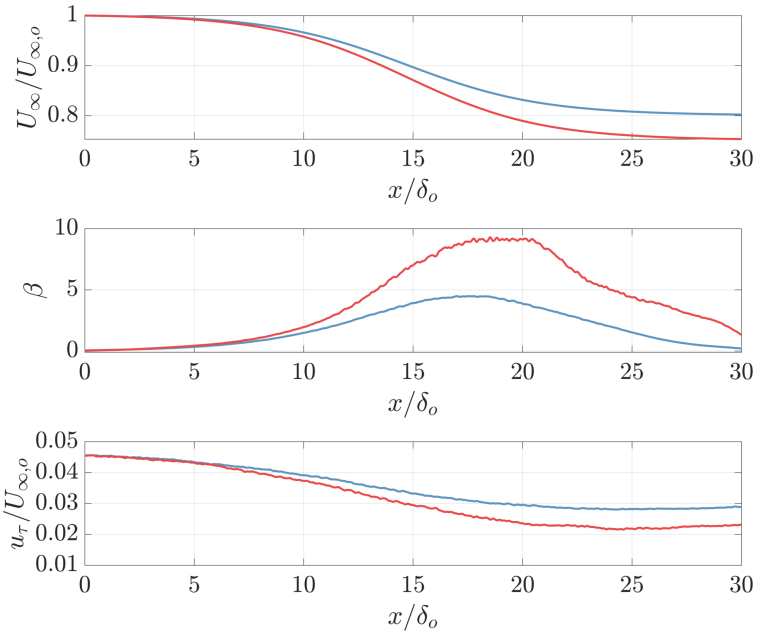

Fig. 1 Profiles of: Top, freestream velocity applied at top boundary $U_\infty(x)$. Middle, Clauser parameter $\beta = (\delta^*/\tau_w)(dP/dx)$ over the smooth wall. Bottom, friction velocity over the smooth wall. —— *B*5**;** —— *B*10**.**

that the freestream-induced deceleration influences the TBL gradually rather than abruptly altering the inflow TBL; 2) allow significant streamwise distance for the boundary layer to develop under the APG; 3) prevent the region of interest from being impacted by the convective outflow. L_z is about $5\delta_o$ with slight adjustment between cases to ensure exact periodicity of the riblet sinusoid (between 27 to 99 riblet spanwise periods depending on the size of the riblet). $L_y \approx 5\delta_o$ is set such that the freestream boundary on the top is far enough to allow the boundary layer to develop freely during the deceleration without significant blockage.

B. Riblet configuration

For each of the discussed APGs, streamwise-aligned riblets are applied on the bottom wall of the domain. All the riblets examined in this study share the same sinusoidal form as a function of the spanwise coordinate (z):

$$h_l(z) = 0.5h\left[\sin\left(2\pi z/s\right) + 1.0\right], \tag{2}$$

where h is the maximum riblet height measured from the lowest point in the valley and s is the peak-to-peak spanwise spacing. In this study, the ratio h/s is fixed to be $3/\pi$. Another commonly used riblet length scale is

$$l = \sqrt{hs - \int h_l dz} \tag{3}$$

the square root of the groove cross-section area (see figure 2). It has been shown to predict drag modulation by a variety of riblet shapes, exhibiting greater universality among geometries than s^+ [13–15]. For the present sinusoidal geometry, l is directly related to s (and therefore to h) through $\sqrt{3/(2\pi)}s$, such that specifying one immediately determines the others. Consequently, the chosen riblet shape admits only a single geometric degree of freedom.

Three riblet sizes characterized by these length scales are chosen to lie near the critical thresholds established in ZPG flows (refer to Table 1). The smallest one is chosen to be $l_o^+ \approx 11$ ($s_o^+ \approx 16$, $h_o^+ \approx 15$), which is the optimal drag-reducing size widely reported in ZPG flows [2, 9, 13–15]. The medium size is $l_o^+ \approx 18$ ($s_o^+ \approx 26$, $h_o^+ \approx 25$), where drag penalty by riblets in ZPG flows begins with the occurrence of KH roller vortices near the crest of the riblets (for certain riblet shapes, see figure 15(c) in the study by Endrikat *et al.* in Ref. [33], as well as Refs. [13, 14, 34]). The largest riblet size is chosen as $l_o^+ \approx 41$ ($s_o^+ \approx 60$, $h_o^+ \approx 57$). At this size, drag penalty in ZPG flows is no longer affiliated with spanwise rollers, and is rather due to the descent of turbulence into the riblet grooves [33, 35, 36]. Relative to the

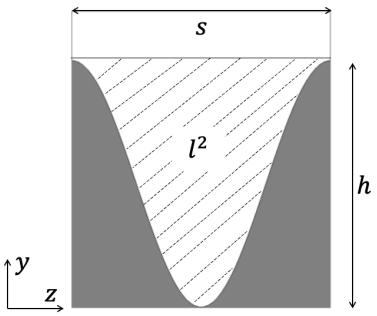

Fig. 2 One spanwise period of the sinusoidal riblet profile with spanwise spacing (s), wall-normal height (h), and groove cross-sectional area (l^2) labeled.

Table 1 Simulation Parameters. See text for variable definitions.

Case	l_o^+	max (β)	$\left[L_x, L_y, L_z\right]/\delta_o$	$\left[n_i, n_j, n_k\right]$	Periods	n_h	n_s	$\Delta y^+_{1,o}$	Δx_o^+	Δz_o^+
B05l00	-	5	[55.3, 4.9, 4.9]	[1980, 270, 660]	-	-	-	0.14	9.1	2.3
B10l00	-	10	[55.3, 4.9, 4.9]	[1980, 270, 660]	-	-	-	0.14	9.1	2.3
B05l10	11	5	[57.7, 4.9, 4.8]	[2112, 296, 1584]	99	54	16	0.13	8.8	0.9
B10l10	11	10	[57.7, 4.9, 4.8]	[2112, 296, 1584]	99	54	16	0.13	8.8	0.9
B05l20	18	5	[56.0, 4.9, 4.8]	[2016, 270, 1512]	54	54	28	0.47	8.9	0.95
B10l20	18	10	[56.0, 4.9, 4.8]	[2016, 270, 1512]	54	54	28	0.47	8.9	0.95
B05l40	41	5	[58.3, 4.9, 4.9]	[2160, 309, 1080]	27	100	40	0.58	9.9	1.5
B10l40	41	10	[58.3, 4.9, 4.9]	[2160, 309, 1080]	27	100	40	0.58	9.9	1.5

reference location boundary layer thickness, the riblet sizes are: $l/\delta_o \approx 0.034$, 0.056, and 0.128; $s/\delta_o \approx 0.049$, 0.088, and 0.181; and $h/\delta_o \approx 0.047$, 0.084, and 0.172.

By selecting riblet sizes near these critical thresholds in the ZPG region preceding the APG, we aim to characterize potential changes in drag modulation, and the associated mechanisms, due to the deceleration. Specifically, since u_τ decreases under an APG, the $l_o^+ = 11$ ($s_o^+ = 16$) case is expected to exhibit reduced drag reduction, with no KH rollers present throughout the domain. The $l_o^+ = 18$ ($s_o^+ = 26$) case is anticipated to achieve greater drag reduction, with KH rollers showing near the reference plane and diminishing as l^+ decreases below the threshold of 20. For the $l_o^+ = 41$ ($s_o^+ = 60$) case, a change from drag augmentation to drag reduction by the APG is expected, and although KH rollers are not anticipated at the reference location, they may develop downstream as l^+ further decreases under the influence of the APG.

The combination of two APG levels and three riblet sizes produces six riblet configurations, complemented by two smooth-wall baseline cases. We name each case in the format of 'BXXlYY', where 'B' denotes the maximum β value for the two APGs. 'XX' = 05 corresponds to the weaker APG with maximum $\beta \approx 5$, while 'XX' = 10 corresponds to the stronger APG with maximum $\beta \approx 10$. 'l' denotes the value of l_o^+, with 'YY' = 00, 10, 20, and 40 corresponding to the smooth wall, and riblets with $l_o^+ \approx 11$, 18, and 41, respectively.

C. Numerical methods

The incompressible Navier-Stokes equations

$$\nabla \cdot \mathbf{u} = 0; \ \frac{\partial \mathbf{u}}{\partial t} + (\mathbf{u} \cdot \nabla)\mathbf{u} = -\nabla p + \nu \nabla^2 \mathbf{u} + \mathbf{f} \tag{4}$$

are solved by DNS. Here, p is modified pressure, and $\mathbf{f}$ is the immersed boundary method (IBM) force used to enforce the no-slip boundary condition on the riblets. The IBM is based on the volume-of-fluid (VOF) approach [37, 38]. In the pre-processing stage, the fractional volume of each computational cell occupied by fluid is calculated. During the

simulation, the predicted velocity at each time step is weighted by such a fraction and then corrected to be divergence-free via pressure projection, thereby enforcing the no-slip condition. The body force $\mathbf{f}$, which represents the force required to bring the fluid to rest within the solid region, accounts for all forces induced by the embedded structure. Because of the streamwise alignment of the riblets, only skin friction contributed to $\mathbf{f}$. Wall-normal integration of $\mathbf{f}$ provides the total wall stress at each location. Readers are referred to Refs. [39, 40] for detailed proofs regarding the relationship between the IBM force and wall stresses.

A Cartesian mesh is designed for each case to resolve the motions of various scales, including those on the sub-riblet scales. The x grid is uniform throughout until $x/\delta_o = 24$, and linearly stretched near the outflow with a stretch ratio less than 3%. The y grid is kept uniform below the riblet crest, with n_h points resolving the riblet height. n_h is varied between cases to ensure that $\Delta y^+_{(1)} \leq 0.6$ in all cases (see Table 1). Above the riblet crest, the y grid is stretched using a hyperbolic-tangent profile with a stretch ratio less than 3%. The z grid is uniform, with n_s points resolving a riblet period. n_s is adjusted between cases to ensure that the viscous scale of turbulence and the sub-riblet scale flow are resolved (also listed in Table 1. Since u_τ decreases in the streamwise direction, the reference plane represents the location with the coarsest grid resolution in wall units. Nevertheless, the resolution achieved there is comparable to, or better than, that of previous DNS studies on turbulent channel flows over riblets (refer to Table 1).

The DNS is performed using a well-validated, in-house finite difference code [41–43], which solves the equations of motion on a staggered grid. Second-order-accurate central differences are used for all spatial derivatives. Time is advanced using a fractional step method [44]. Time is discretized semi-implicitly, with the wall-normal diffusion and the pressure gradient terms treated with the implicit Crank-Nicolson scheme, while all remaining terms are treated with an explicit Adams-Bashforth scheme. The Poisson equation is solved using a pseudo-spectral technique [45]. The code is parallelized using the message-passing interface (MPI) protocol.

D. Statistics collection and data reduction

Statistics are collected after the flow in each case reaches a statistically steady state. The total sample time is $100\delta_o/U_{e,o}$. The full three-dimensional flow field is saved every $0.36\delta_o/U_{e,o}$ and select two-dimensional planes saved every $0.15\delta_o/U_{e,o}$.

For the smooth-wall cases, quantities are decomposed using the canonical Reynolds decomposition: $\phi(x,y,z,t) = \left\langle \overline{\phi} \right\rangle (x,y) + \phi'(x,y,z,t)$, where the operators $\overline{(.)}$ and $\langle . \rangle$ denote the temporal and spanwise average, respectively. $(.)'$ denotes the stochastic turbulent fluctuations. For the riblet cases, instantaneous quantities are first decomposed with a dispersive field, obtained by averaging in time and ensemble averaging over repeated riblet periods. Then, together with the local stochastic turbulent fluctuation as the residual, the decomposition reads: $\phi(x,y,z,t) = \overline{\phi}(x,y,z_r) + \phi'(x,y,z,t)$. Here, $z_r = \mathrm{mod}(z,s) \in [0,\ s)$ is the spanwise location within a riblet period corresponding to the global z location. The dispersive field is then decomposed into a spanwise average over the riblet and the spatial variation about this average: $\overline{\phi}(x,y,z_r) = \left\langle \overline{\phi} \right\rangle (x,y) + \tilde{\phi}(x,y,z_r)$. This yields the 'double average' widely employed in rough- and riblet-wall turbulence literature [15, 33, 46–48]:

$$\phi(x,y,z,t) = \left\langle \overline{\phi} \right\rangle (x,y) + \tilde{\phi}(x,y,z_r) + \phi'(x,y,z,t). \tag{5}$$

For the operators introduced by this decomposition, those without a subscript denotes the intrinsic spanwise average over the fluid domain only, whereas $\langle . \rangle_s$ indicates the superficial spanwise average over the fluid and solid domains. Throughout this paper, temporally and spanwise ensemble-averaged primary variables are represented by capital letters as well.

III. Results

A. Boundary layer development

The mean velocity is compared in figure 3. The boundary layer thickness is indicated by the white dashed line, and the riblet crest is represented by the black horizontal line. It can be seen that the APG decelerates and thickens the boundary layer and the extent of thickening varies between the cases. This is quantified by β and $Re_\delta = \delta U_e/\nu$ in the top two rows of figure 4. The maximum value of β increases dramatically with riblet size. For the largest riblet under the moderate APG (case B05l40), and the two largest riblets under the strong APG (B10l20, B10l40), β approaches infinity shortly after the APG takes into action. This trend reflects a rapid deceleration near the wall (i.e., within the riblet region). However, the deceleration further away from the wall remains largely unaffected, resulting in negligible

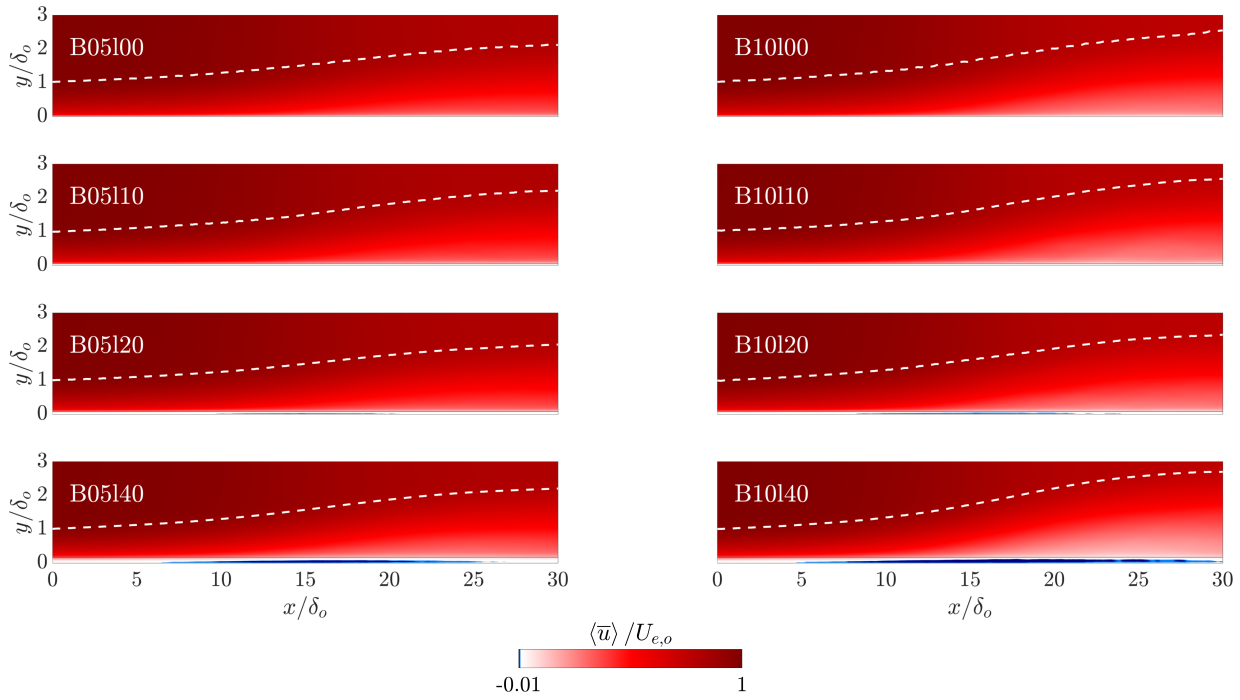

Fig. 3 Contours of the time- and spanwise-averaged streamwise velocity. The superimposed white dashed lines denote δ, while the thin horizontal black line denotes the riblet crest. The spanwise average is intrinsic (i.e., over the fluid domain only) below the riblet crest. Note that the blue (reverse flow) and red (forward flow) regions are saturated at different magnitudes, with white representing zero velocity as the pivot.

increases in Re_δ for all moderate-APG cases and the high-APG cases with small or medium riblets.

For two-dimensional separating flow over smooth walls, infinite β, resulting from wall shear stress approaching zero, serves as a necessary and sufficient indicator of flow separation. However, this criterion does may apply to surfaces with microstructures. A previous study on separating flows over sandgrain roughness by Wu & Piomelli [49] demonstrated that reverse flow can occur within the roughness layer, producing zero or even negative wall shear stress well before separation occurs in the outer flow. A similar phenomenon is observed in the present study. The mean velocity contours clearly show the formation of a mean reverse flow within the riblet grooves, most prominently in cases B05l20, B05l40, B10l20, and B10l40. The wall shear stress and mean velocity at the riblet crest are shown in the bottom two rows of figure 4. It can be seen that three cases - B05l40, B10l20, and B10l40 - exhibit negative wall shear stress after being decelerated by the APG. However, none of the cases display a negative mean velocity at or above the riblet crest. Therefore, in all cases, the flow continues downstream along the riblet crests (i.e., no flow detachment), while reverse flow develops within the riblet grooves. As we will explain momentarily, this mean reverse flow is due to the generation and passage of consecutive spanwise vortices.

B. Drag reduction quantification

As our primary focus, we quantify the drag change by comparing the smooth-wall and riblet cases. Note that drag reduction should be evaluated by comparing two flows that either have the same mass flow rate but differ in wall shear stress, or share the same wall shear stress but differ in flow rate. In the current study, Re_δ remains nearly the same between the smooth and riblet cases at each streamwise location in most cases. Therefore, we compare wall shear stress values at the same x position to evaluate drag differences.

In ZPG flows, the drag modulation by riblets is predicted by the 'drag curve', which plots $\Delta\tau_w$ versus viscous-scaled riblet size, typically l^+ (e.g., figure 5 in Ref. [14]). $\Delta\tau_w$ is defined as:

$$\Delta\tau_w(x) = 100 \times \frac{\tau_{w,\mathrm{r}}(x) - \tau_{w,\mathrm{s}}(x)}{\tau_{w,\mathrm{s}}(x)}\text{‰}, \tag{6}$$

where subscripts 'r' and 's' denote the riblet and smooth wall, respectively. Figure 5 presents our results alongside those

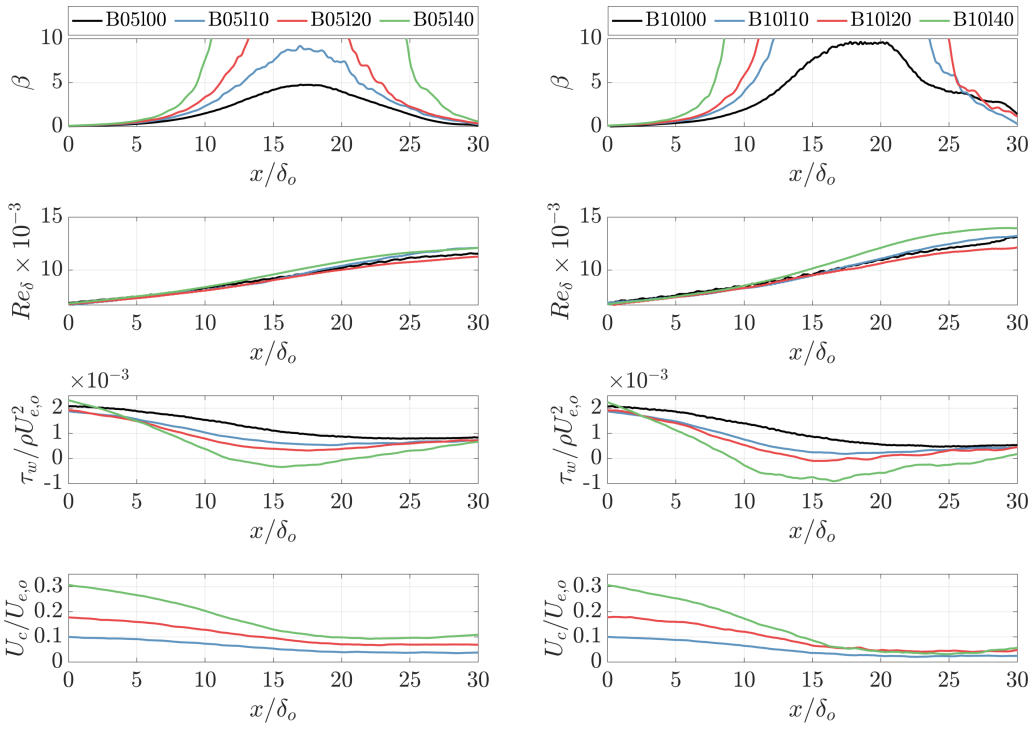

Fig. 4 Streamwise development of various boundary layer parameters. From top to bottom: Clauser parameter ($\beta = (\delta^*/\tau_w)(dP/dx)$); $Re_\delta = \delta U_e/\nu$; wall shear stress ($\tau_w = \nu\partial\langle\overline{u}\rangle/\partial y$ in the smooth wall cases, see text for method of calculation in the riblet cases); mean streamwise velocity at the riblet crest ($U_c/U_{e,o}$). The left column compares the cases at the lower APG and the right column at the higher APG. In all plots, —— l00 (smooth); —— l10; —— l20; —— l40.

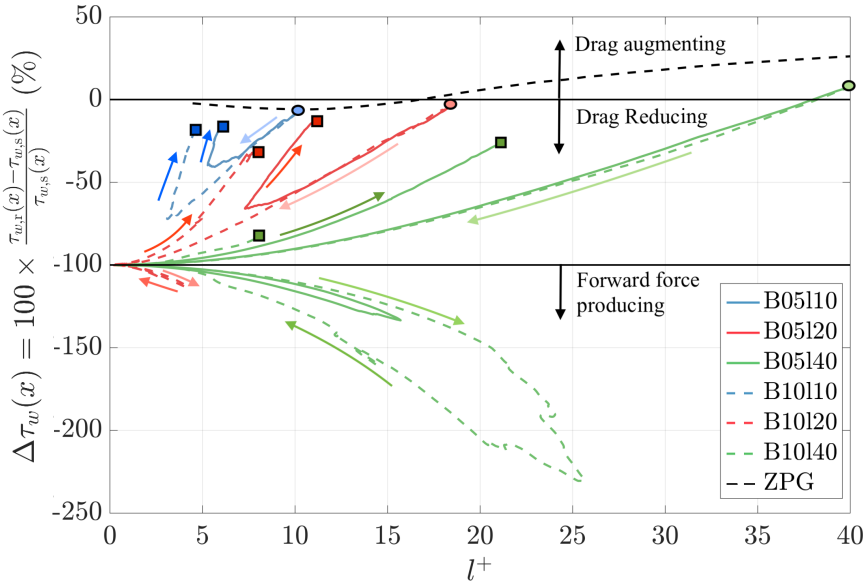

Fig. 5 Drag curve for APG cases compared with the ZPG one of Ref. [50]. The arrows along the APG drag curves indicate the downstream direction, while the darkening shades of color represent locations further downstream. The beginning and end of the region of interest ($x = 0$ and $x/\delta_o = 30$) are indicated by circular and square markers, respectively. Drag augmenting, drag reducing, and forward force producing regimes are indicated.

from the ZPG flow of Ref. [50]. Striking differences, highlighting the non-equilibrium effects, are clearly shown. The circular marker at the beginning of each of the plot is at the reference plane, while the square indicates where $x/\delta_o = 30$. The weaker APG (B05) cases are shown with the solid lines, while the stronger APG (B10) cases are shown with dashed lines. The line colors representing the riblet size at $x = 0$ are the same as figure 4. The drag curve from the ZPG flow of Ref. [50] is given by the dashed black line for reference.

Based on the drag curve of the ZPG flows, we were expecting to see the following changes: the optimal riblet (i.e., l10) cases are designed to be near the optimum of the drag curve, and thus should transit leftward into the viscous, linear regime as u_τ (and thus l^+) decreases by action of the APG. While they should still be drag reducing, drag will be reduced by less than at the inflow since l^+ is below the optimal and thus the riblets have lesser influence on the overlying turbulence. Similarly, the medium riblet (l20) cases should transit from the rightmost end of the drag-reducing regime toward the optimum (i.e., drag will be reduced by a greater percentage downstream of the reference location), while the l40 cases should transit from the drag-increasing regime toward the drag-reducing regime. These trends were expected to be enhanced at the higher APG if the ZPG mechanisms of riblet drag modulation are still valid. The ZPG-based prediction does hold at the reference plane in all cases where the flow is under ZPG conditions. Here, the l10 cases decrease τ_w by $\sim 6\%$, the l20 cases produce near-equal drag, and the l40 cases display a drag increase.

However, our results show significant deviation from this ZPG-based anticipation when the TBL is under APG. As the APG becomes appreciable, l^+ decreases considerably. In all cases, this comes with a multifold augmented drag reduction compared to the ZPG region, and there is significant deviation from the ZPG drag curve (shown by the faint arrows in the figure). Specifically, the prediction for the l10 cases that $\Delta\tau_w$ would increase does not hold. Furthermore, while greater drag reduction was expected for the l20 and l40 cases due to the decrease of l^+, $\Delta\tau_w$ appears to decrease with l^+ significantly faster than predicted by the ZPG drag curve. The behavior of all drag curves are qualitatively similar: $\Delta\tau_w$ decreases with l^+ to a local minimum, after which it begins to increase toward the ZPG drag curve. It was found that the local minimum on the drag curve occurs near peak β ($x/\delta_o \approx 18$), after which recovery toward the equilibrium curve begins as the APG weakens. The trend of the plots towards the end of the computational domain indicates that if given sufficient streamwise recovery distance under the new ZPG state after deceleration, the wall stress may recover to the ZPG drag curve.

Quantitatively, both riblet size and maximum APG strength influence the drag curve characteristics. As riblet size increases, the maximum drag reduction achieved in the peak APG region also increases. For a fixed riblet size and increasing APG strength, the larger APG also results in increased drag reduction. Interestingly, the decrease of $\Delta\tau_w$ with respect to l^+ during the APG onset occurs at the same rate for a given riblet size (i.e., $d\Delta\tau_w/dl^+ \approx$ constant, and the solid and dashed lines collapse before they reach their individual minimum). With the increase of either riblet size or APG strength, the drag curve approaches the point of total drag elimination more closely (i.e., $\Delta\tau_w \to -100\%$). For certain combinations tested here (cases B05l40, B10l20, and B10l40), a region of forward force, or thrust, is indicated by $\Delta\tau_w < -100\%$ where $\tau_{w,r} < 0$. The l^+ resulting from the reverse flow in such region is about 15.

While augmented drag reduction by riblets in very weak APGs relative to ZPG has been reported [22–24], $\Delta\tau_w$ was never reported to exceed -15%. To the best of our knowledge, this is the first report of significant drag reductions, as well as the forward-force regime of the drag curve, under APG effects. The observed deviation from the ZPG drag curve, and range of $45 - 250\%$ drag decrease, suggest that the current mechanisms responsible for drag modulation differ from those in ZPG and near-equilibrium APG TBLs. Therefore, corrections to the present ZPG metrics are likely necessary to predict the riblet influence on skin friction in spatially developing, non-equilibrium APG TBLs.

C. Discussion on skin friction modulation

The deviation between the drag modulation predicted by the ZPG drag curve and the ones generated by the APG indicate that the fundamental drag modulation by riblets differs when the flow is under strong APGs versus ZPG conditions. We now characterize potential mechanisms for the highly reduced, and even negative, τ_w. Since riblets do not generate form drag, the skin friction induced by reverse flow within the grooves is the only motion that can potentially bring the total drag to zero. Positive drag still arises from the mean shear, $\partial U_c/\partial y$, near the riblet crest. For the net drag to vanish, the reverse flow within the grooves must be strong enough to counteract this (APG-weakened) mean shear. This compensation can occur in two ways: by increasing the magnitude of the reverse flow, and/or by expanding the portion of the groove exposed to reverse rather than forward flow. Our data shows both phenomena play a role. The mean streamwise velocity profiles are compared at various streamwise locations in figure 6. For the riblet cases, the wall-normal coordinate is shifted by the riblet height (h). For all riblet cases, reverse flow beneath the riblet crest is observed as early as $x/\delta_o = 10$ and 20. Larger riblets and stronger APG not only induce a stronger reverse flow

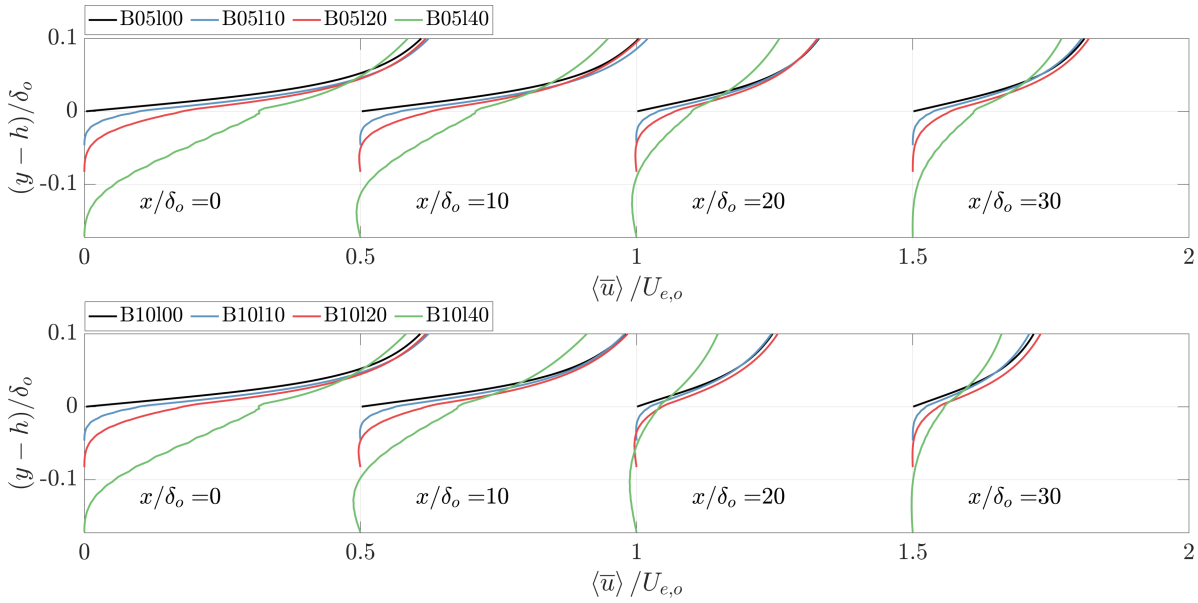

Fig. 6 Mean streamwise velocity profiles extracted at $x/\delta_o = 0$, 10, 20, and 30. The top plot displayed the B5 cases, and the bottom displayed the B10 cases. Color indicates riblet size, as in figure 4. The vertical coordinate is shifted by $1.0h$ for the riblet case such that the riblet crest corresponds to $(y-h) = 0$. Profiles are shifted right by 0.5 units at each x location for clarity.

within the grooves, but also drive it deeper into the groove, increasing the 'wetted' area exposed to the reverse flow.

D. Characterization of KH rollers vortices

To the best of our knowledge, this is the first observation of a *mean* reverse flow beneath riblet grooves that significantly reduces wall shear stress. It has, however, been observed in APG flows over other surface structures such anisotropic porous media, and is attributed with significant drag reduction relative to smooth walls [42]. In ZPG flows over riblets, only local and instantaneous regions of reverse flow—resulting in intermittent yet coherent negative wall shear stress—have been reported under certain conditions [33, 35, 51, 52]. These events are more prominent than the rare reverse flows caused by extreme ejections in canonical TBLs. Owing to their spanwise coherence, they have been linked to the formation of Kelvin–Helmholtz (KH) roller vortices induced by riblets of specific shapes and sizes. However, riblets which induce a KH instability strong enough to form KH rollers have been shown to increase the mean τ_w relative to the smooth wall rather than decreasing it, despite local instantaneous regions of $\tau_w < 0$ [13, 14, 33, 35, 51, 52]. A reduction in mean τ_w by KH rollers, as observed in the present study, has not been previously reported. Our results demonstrate that the reverse flow within the riblet grooves is generated by a train of downstream-traveling KH roller vortices. The temporal averaging of these passing vortices yields a mean reverse groove flow. Figures 7 and 8 show the footprints and streamwise pattern of the rollers in the present cases.

Note that empirical quantitative thresholds for the occurrence of KH rollers over riblets have been developed for ZPG flows, along with explanations based on the behavior of transverse flows within the riblet grooves. In general, KH rollers are not typically observed when riblet geometries are within the drag-reducing regime of ZPG flows. According to Ref. [35], KH rollers can form over riblets for (approximately) $l^+ \in [15,\ 40]$, given that the cross-sectional shape is proper to generate strong shear near the riblet crest (see figure 15(c) of the cited study). As mentioned in Section II.B, the riblets are designed in the current study such that the l10 cases live below this regime, and the decrease of u_τ and l^+ by the APG should further hinder the formation of KH rollers. The l20 cases are designed to be near the low end of the necessary size, and thus l^+ should decrease below the KH roller-sustaining regime during the APG. Finally, the l40 cases are designed so that l^+ transits into the KH roller-sustaining regime during the APG.

Figure 7 exhibits that there are clear spanwise-coherent regions in all cases consisting of alternating forward and reverse flow. Such contours are reminiscent of the regions of instantaneous reverse shear stress in Refs. [35, 51, 52], suggesting the presence of KH rollers in the present study. Roller vortex presence is further suggested by instantaneous

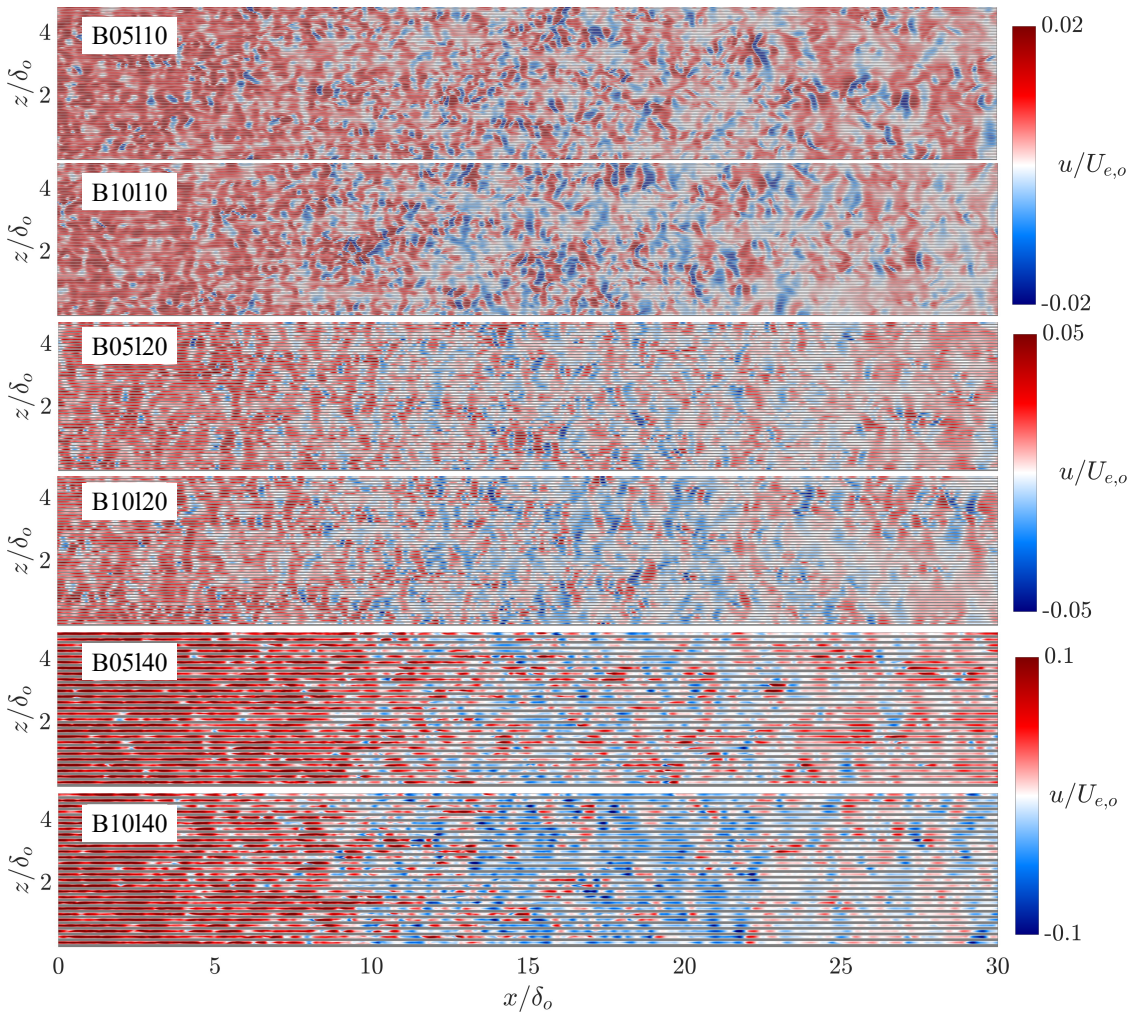

Fig. 7 Instantaneous streamwise velocity contours in the $x-z$ plane at the half-riblet height. The top two figures are the l10 cases, the middle two are the l20 cases, and the bottom two are the l40 cases. Note the different color scaling for the different riblet sizes. Regions occupied by the riblets are shaded in gray.

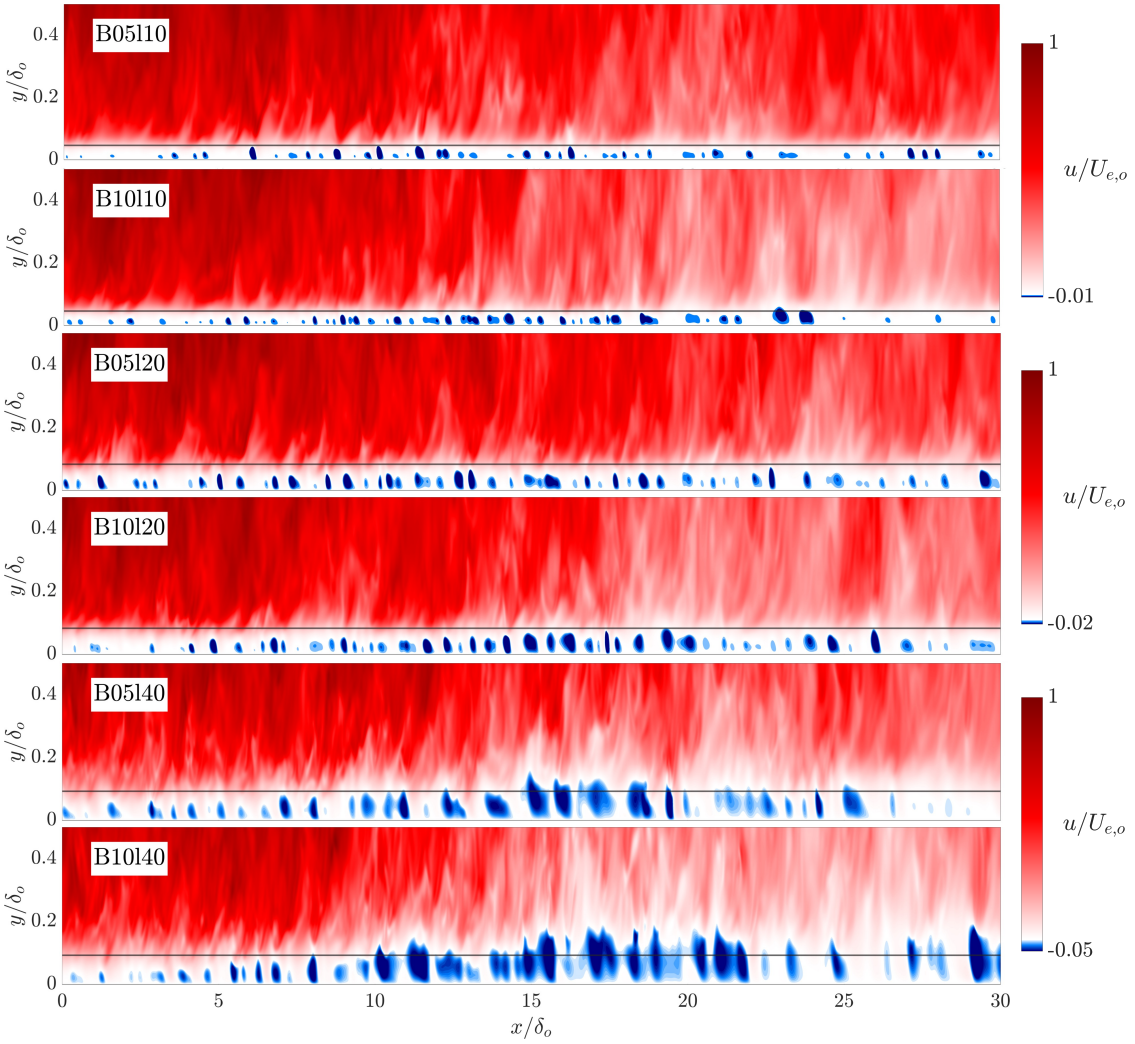

Fig. 8 Instantaneous streamwise velocity contours in the $x-y$ plane taken at the spanwise location of a riblet trough. The top two figures are the l10 cases, the middle two are the l20 cases, and the bottom two are the l40 cases. The solid horizontal line denotes the height of the riblet crest. Note the varying color scales used for different riblet sizes, as well as the vertical axis stretching applied to enhance the clarity of the near-wall region.

streamwise velocity in the $x - y$ plane taken in the riblet groove, as provided in figure 8. The KH rollers are readily identified by quasi-circular regions of reverse flow below the riblet crest height. It is evident that for increasing riblet size at a fixed APG, the strength of the KH rollers, and their size increase. The same is true for increasing APG strength at a fixed riblet size.

Recall that the riblet sizes were chosen specifically to examine the occurrence and evolution of the KH rollers. For the small riblets (l10, top two rows of figure 7), weak spanwise coherence is observed near the inlet. This agrees with previous findings, as such small riblets are known to support only weak and relatively incoherent KH rollers [14, 35]. However, further downstream, as the APG strengthens and l^+ decreases — conditions under which KH rollers are less likely to form according to ZPG-based thresholds and explanations — the rollers not only persist but also grow in coherence and intensity. Our cases show alternating regions of forward and reverse flow with notable spanwise coherence, suggesting that the KH rollers intensify even as l^+ decreases under APG. For the l20 cases (middle two rows of figure 7), spanwise-coherent structures are evident throughout the entire domain. While the formation of rollers at the ZPG reference location was anticipated, they were expected to weaken downstream as the APG reduces l^+, based on findings from ZPG flows. However, similar to the l10 cases, both the coherence and the strength of the reverse flow increase in the downstream direction as the APG develops. Compared to the l10 cases, the l20 cases exhibit stronger reverse flow, greater spanwise coherence, and longer streamwise wavelengths.

Finally, in the l40 cases (bottom two rows of figure 7), the signature of KH rollers is not evident at the reference plane as expected. Then, spanwise-coherent regions of intense reverse and forward flow form as the APG grows. While this aligns with expectations based on findings from ZPG flows, the failure of such predictions for the l10 and l20 cases raises questions about the validity of the explanation in previous studies on the occurrence of the KH rollers when the TBL departs from its self-similar state under APG. The spanwise coherence is arguably less than the l20 riblets. This is likely due to the oversized riblets permitting turbulence to penetrate into the grooves and disrupt the KH rollers, whereas smaller riblets lift near-wall streaks and flow in the grooves is viscous-dominated. However, the intensity of the reverse flow, and the streamwise wavelength of the presumed KH rollers are larger in the l40 cases than in the l10 and l20 cases, thereby explaining the monotonic growth of mean reverse flow with increasing riblet size (refer to figure 6).

E. Discussion about KH rollers vortices

Our results indicate that the mean reverse groove flow arises from the passage of KH roller vortices, whose lower halves induce a local flow reversal through their negative velocity. Since the bulk flow carrying these vortices continues downstream, the resulting mean reverse flow is, in a sense, a 'pseudo' (or traveling local) reversal rather than a true upstream bulk motion. More importantly, the previously established thresholds and explanations for the occurrence of KH rollers may not hold in non-equilibrium TBLs. Moreover, rather than causing drag augmentation, KH roller vortices can actually reduce drag if they are sufficiently strong and prevalent enough to generate a sustained mean reverse flow within the riblet grooves.

Comparing the cases, it is found that the magnitude of the spanwise-coherent reverse flow increases with APG strength as well as the riblet size, while the proportion of forward flow within the riblet groove decreases (this is most noticeable comparing case B05l40 with B10l40 in figure 7). It is also interesting to observe the spatial evolution of KH rollers. That is, the streamwise wavelength of the rollers appears to increase with downstream distance. Most notably, in the region of strong APG ($10 \lesssim x/\delta_o \lesssim 25$), the streamwise width of the reverse flow regions tends to increase relative to the upstream quasi-ZPG region. Such spatial development of KH rollers has not been observed in ZPG riblet flows. These observations may indicate a more frequent generation of the KH rollers, stronger KH rollers, or slower convective speed that causes the cluster of consecutive vortices.

There are three physical scenarios which could result in the large rollers observed in the strong APG region. First: the relatively small KH rollers generated in the upstream quasi-ZPG region grow as they convect downstream. Second: the rollers are generated locally, and the APG results in local flow conditions that yield larger rollers than in ZPG flows. Third: the convective velocity of the rollers generated in the quasi-ZPG region slows due to the APG, resulting in merging of successive rollers. As a preliminary assessment of these potential mechanisms, figure 9 shows the space-time map of the strong instantaneous reverse flow (isosurfaces of $u(x, y)/U_{e,o} = -0.01$ sampled at an $x - y$ plane located at a riblet trough at successive time instances). Note that the other riblet sizes and larger APG cases exhibited qualitatively similar vortex evolution (quantitative differences exist in streamwise wavelengths per riblet size and convective velocities per APG strength), thus only case B05l40 is shown here. The isometric plot is oriented such that the roller convective speed (c_{KH}) at x/δ_o is vertical. Faster motions are then inclined rightward, while slower motions are inclined leftward.

Addressing first scenario above, the rollers are convecting at $c_{\mathrm{KH}}/u_{\tau,o} \approx 5$ at $x/\delta_o = 0$, consistent with wave

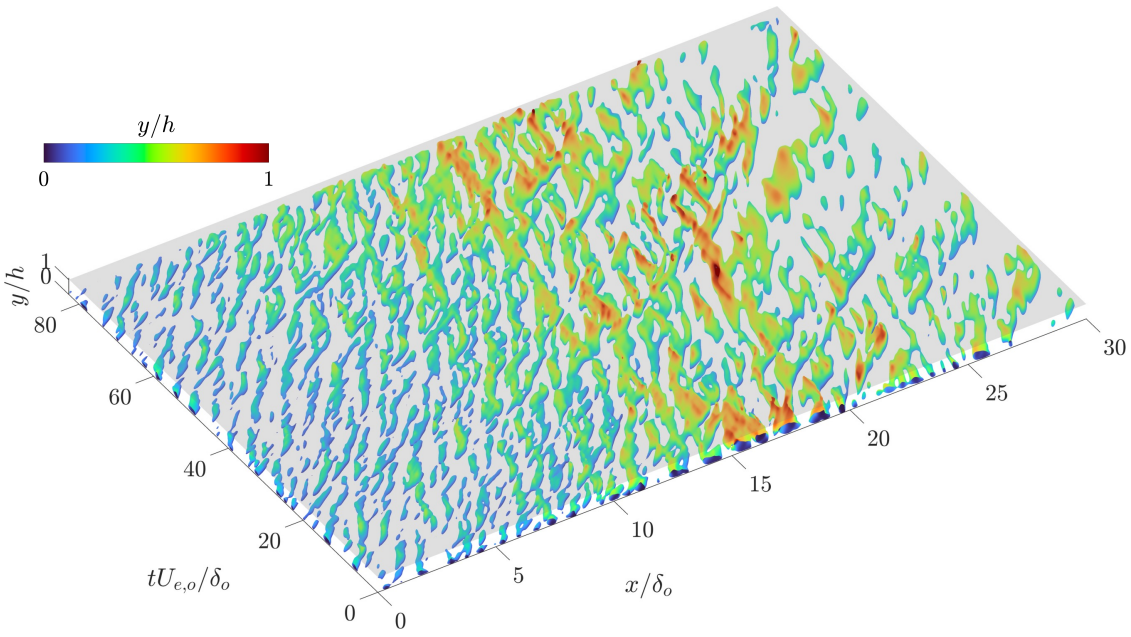

Fig. 9 Time evolution of spanwise rollers for case B05l40. Isosurfaces of instantaneous $u/U_{e,o} = -0.01$ are generated by stacking time-resolved samples of the $x-y$ plane at a riblet trough. The resulting surface represents the temporal evolution of intense reverse-flow regions. Coloring indicates the wall-normal distance from the riblet trough. The gray horizontal plane marks the riblet crest height.

speeds measured in previous DNS studies and predicted by linear stability analysis [14, 33, 35, 36]. However, our data suggests that the rollers do not convect downstream un-disturbed into the APG region. Rather, they have a finite lifespan and are distorted by the overlying turbulence which convects downstream at $c_t/u_{\tau,o} \approx 15$, again consistent with previous studies. The second scenario, meanwhile, appears evident in figure 9: the large rollers in the strong APG region ($x/\delta_o \approx 15$) are generated locally, and their increased size relative to those in the ZPG region is likely dependent on local flow conditions. Finally, the third scenario is also (partially) true: the rollers generated in the APG region convect downstream slower than those in the ZPG region. They additionally have a longer livespan than those upstream. While successive vortices do merge, this does not appear to be the dominant cause of such large structures. The combination of the large, locally-generated rollers, their slower convective velocity, and their increased lifespan results in temporally-averaged reverse flow and the reduced shear stress previously observed.

To investigate why the rollers are larger in the strong APG region, we assess the evolution of the vorticity thickness:

$$\delta_\omega = (U_{\max} - U_{\min})/(\partial \langle \overline{u} \rangle / \partial y)_{\max}, \tag{7}$$

where $U_{\min}$ and $U_{\max}$ are the minimum and maximum intrinsically-averaged streamwise velocity at each x location, and $(\partial \langle \overline{u} \rangle / \partial y)_{\max}$ is the maximum local velocity gradient (which occurs at the riblet crest in all cases). δ_ω/δ_o is shown in figure 10. In all cases, δ_ω grows as the APG takes action, primarily due to the decrease of maximum $(\partial \langle \overline{u} \rangle / \partial y)_{\max}$, as shown in the middle row of figure 10. While the decrease of velocity gradient intuitively suggests that rollers are less likely to form, the growth of δ_ω suggests that if conditions are sufficient for rollers to form, their wavelength will be larger in the APG region than in the ZPG region. Further, because this increase is more pronounced in the B10 cases, larger rollers are expected for the larger APG, as we have observed.

It is noted that δ_ω/δ_o grows with physical riblet size, providing an indication that larger riblets permit the growth of larger rollers. That said, maximum velocity gradient decreases monotonically with riblet size, suggesting rollers are less likely to form for the larger riblets. However, when the maximum velocity gradient is normalized as the gradient over the riblet height (bottom row of figure 10), as physical riblet size is responsible for determining the extent of the 'shear layer' (since the inflection point occurs at the riblet crest) and thus the size of the rollers, it is observed that the shear increases with riblet size. This, combined with the growth of vorticity thickness with riblet size, provides indication as to why the rollers and thus mean reverse flow also grow with riblet size. Again, it is assumed that while the shear decreases in x due to the APG, it remains sufficient to generate rollers.

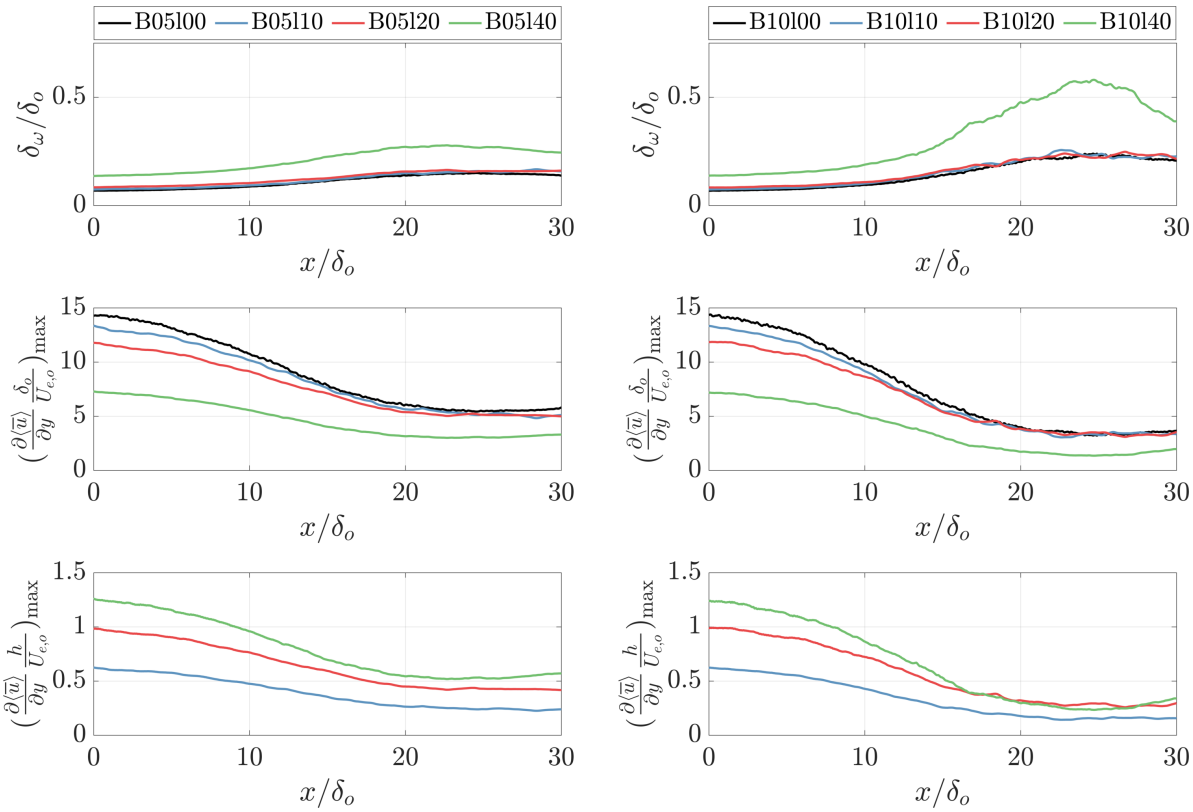

Fig. 10 Top row: vorticity thickness (δ_ω/δ_o). Middle row: maximum velocity gradient normalized by reference boundary layer thickness and freestream velocity. Bottom row: maximum velocity gradient normalized by riblet height and reference freestream velocity. Left and right columns show the weaker (B05) and stronger (B10) APG cases, respectively. Riblet size is indicated by line color, as in previous figures.

Previous studies of spanwise rollers over riblets in ZPG flows attribute their formation and size to a combination of wall-normal transpiration near the riblet crest (which occurs when the riblets are larger than those typically used for drag reduction) as well as high shear generated at the crest to form an inflection point in the mean velocity profile [33, 35, 36, 52]. This depends on a delicate balance of: 1) sufficiently large riblets to permit transpiration at the crest, and 2) sufficiently small (and sufficiently shaped) riblets such that turbulence does not penetrate into the grooves and high shear is maintained near the crest. In such equilibrium flows, it was recently shown that the balance between unsteady-inertia and the overlying pressure dictates the relationship between viscous-scaled riblet size and the formation and size of rollers [36]. Our results suggest that the APG sustains an internal shear layer of sufficient strength to enable the roll-up of KH vortices, even when the viscous-scaled riblet size would suggest that such structures should not form. Ongoing work involves determining how APGs modify such delicate balances and promote the growth of such large structures.

IV. Conclusion

In this work, direct numerical simulations of adverse pressure gradient (APG) turbulent boundary layers over riblets are performed. The pressure gradients are selected to produce significant deceleration while avoiding flow detachment. The objective is to determine whether riblets preserve their ZPG drag-reducing benefits in strongly decelerating TBLs and, if deviations occur, to characterize the physical mechanisms governing these changes in drag. Three riblet sizes are examined, placing them in the drag-reducing, drag-increasing, or KH-roller-inducing regimes at the ZPG reference location. Two APG strengths, reaching peak values of $\beta = 5$ and $\beta = 10$ over the smooth wall, are tested. All cases exhibit drag reduction during the APG, and reduction increases with both riblet size and APG strength. The drag reduction achieved during the APG is considerably greater than previously reported in ZPG and mild APG flows.

Accordingly, the drag curve deviates considerably from the well-established ZPG drag curve, indicating that existing ZPG-based metrics require modification when the pressure gradient is non-negligible.

A newly observed feature of the drag curve is the emergence of a 'forward-force' or thrust-production regime for select combinations of riblet size and APG strength. This is indicative of drag reduction by more than 100%. This forward-force-producing regime, along with the significant drag reduction observed in all remaining cases, results from a mean reverse flow beneath the riblet crest, despite the absence of massive flow separation. The mean reverse flow is shown to be generated by traveling Kelvin–Helmholtz (KH) roller vortices whose strength and size increase with the local APG at their generation site. Ongoing work includes stability analysis and investigation of wall-normal admittance to further understand how APGs promote the formation and amplification of these large rollers, and how these structures influence drag modulation.

Acknowledgments

BSS and WW acknowledges the support from AFOSR Grant No. FA9550-25-1-0033, monitored by Dr. Gregg Abate. BSS also appreciates partial support of NSF GRFP Award No. 2235036. AR acknowledges the support from AFOSR Grant No. FA8655-24-1-7008, monitored by Dr. Douglas R. Smith and Dr. Barrett Flake. This work was supported in part by high-performance computer time and resources from the DoD High Performance Computing Modernization Program. Some simulations also used the Expanse supercomputer at the San Diego Supercomputer Center under an ACCESS allocation. The authors gratefully acknowledge these sources of support.

References

[1] Kennedy, J. F., Hsu, S.-T., and Lin, J.-T., "Turbulent flows past boundaries with small streamwise fins," *J. Hydraul. Div. ASCE*, Vol. 99, No. 4, 1973, pp. 605–616.

[2] Walsh, M. J., "Drag characteristics of V-groove and transverse curvature riblets," *Viscous Flow Drag Reduction*, Progress in Astronautics and Aeronautics, Vol. 72, edited by G. R. Hough, AIAA, 1980, pp. 168–184.

[3] Walsh, M. J., *Turbulent boundary layer drag reduction using riblets*, AIAA, 1982, pp. 82–0169.

[4] Walsh, M. J., "Riblets as a viscous drag reduction technique," *AIAA J.*, Vol. 21, 1982, pp. 485–486.

[5] Gallagher, J. A., and Thomas, A. S. W., *Turbulent boundary layer characteristics over streamwise grooves*, AIAA, 1984.

[6] Sawyer, W. G., and Winter, K. G., "The effect of turbulent skin friction of surfaces with streamwise grooves," *European Meeting on Turbulent Drag Reduction*, 1986.

[7] Choi, K.-S., "Near-wall structure of a turbulent boundary layer with riblets," *J. Fluid Mech.*, Vol. 208, 1989, pp. 417–458.

[8] Luchini, P., Manzo, F., and Pozzi, A., "Resistance of a grooved surface to parallel flow and cross-flow," *J. Fluid Mech.*, Vol. 228, 1991, pp. 87–109.

[9] Choi, H., Moin, P., and Kim, J., "Direct numerical simulation of turbulent flow over riblets," *J. Fluid Mech.*, Vol. 255, 1993, pp. 503–539.

[10] Suzuki, Y., and Kasagi, N., "Turbulent drag reduction mechanism above a riblet surface," *AIAA J.*, Vol. 32, No. 9, 1994, pp. 1781–1790.

[11] Goldstein, D., Handler, R., and Sirovich, L., "Direct numerical simulation of turbulent flow over a modelled riblet covered surface," *J. Fluid Mech.*, Vol. 302, 1995, pp. 333–376.

[12] Lee, S.-J., and Lee, S.-H., "Flow field analysis of a turbulent boundary layer over a riblet surface," *Exp. Fluids*, Vol. 30, No. 2, 2001, pp. 153–166.

[13] García-Mayoral, R., and Jiménez, J., "Drag reduction by riblets," *Phil. Trans. R. Soc. A*, Vol. 369, 2011, pp. 1412–1427.

[14] García-Mayoral, R., and Jiménez, J., "Hydrodynamic stability and breakdown of the viscous regime over riblets," *J. Fluid Mech.*, Vol. 678, 2011, pp. 317–347.

[15] Modesti, D., Endrikat, S., Hutchins, N., and Chung, D., "Dispersive stresses in turbulent flow over riblets," *J. Fluid Mech.*, Vol. 917, 2021, p. A55.

[16] Kuntzagk, S., "Aeroshark – Drag Reduction Using Riblet Film on Commercial Aircraft," *Hamburg Aerospace Lecture Series*, AreoLectures, 2024.

[17] Wu, H., Moreau, S., and Sandberg, R. D., "Effects of pressure gradient on evolution of the velocity-gradient tensor invariant dynamics on a controlled-diffusion aerofoil at $Re_c = 150,000$," *J. Fluid Mech.*, Vol. 868, 2019, pp. 584–610.

[18] Pargal, S., Wu, H., Yuan, J., and Moreau, S., "Adverse-pressure-gradient turbulent boundary layer on convex wall," *Phys. Fluids*, Vol. 34, 2022, p. 035107.

[19] Ran, W., Zare, A., and Jovanović, M. R., "Model-based design of riblets for turbulent drag reduction," *J. Fluid Mech.*, Vol. 906, 2021, p. A7.

[20] Smith, B. R., and Yagle, P., "RANS Turbulence Model for Drag Reducing Riblets and Its Predictions for Aerodynamic Applications," *AIAA SCITECH 2025 Forum*, AIAA, 2025, pp. 1–18.

[21] Choi, K.-S., "Effects of longitudinal pressure gradients on turbulent drag reduction with riblets," *Turbulence Control by Passive Means*, edited by E. Coustols, 1990, pp. 109–121.

[22] Nieuwstadt, F. T. M., Wolthers, W., Leijdens, H., Krishna Prasad, K., and Schwarz-van Manen, A., "The reduction of skin friction by rilets under the influence of an adverse pressure gradient," *Exp. Fluids.*, Vol. 15, 1993, pp. 17–26.

[23] Debisschop, J. R., and Nieuwstadt, F. T. M., "Turbulent boundary layer in an adverse pressure gradient: Effectiveness of riblets," *AIAA. J.*, Vol. 34, No. 5, 1996, pp. 932–937.

[24] Klumpp, S., Guldner, T., Meinke, M., and Schröder, W., "Riblets in a turbulent adverse-pressure gradient boundary layer," *5th Flow Control Conference*, AIAA, 2010, pp. 1–11.

[25] Boomsma, A., and Sotiropoulos, F., "Riblet drag reduction in mild adverse pressure gradients: A numerical investigation," *Int. J. Heat Fluid Fl.*, Vol. 56, 2015, pp. 251–260.

[26] Vinuesa, R., Negi, P. S., Atzori, M., Hanifi, A., Henningson, D. S., and Schlatter, P., "Turbulent boundary layers around wing sections up to $Re_c = 1,000,000$," *Int. J. Heat Fluid Fl.*, Vol. 72, 2018, pp. 86–99.

[27] Tanarro, Á., Vinuesa, R., and Schlatter, P., "Effect of adverse pressure gradients on turbulent wing boundary layers," *J. Fluid Mech.*, Vol. 883, 2020, p. A8.

[28] Lund, T. S., Wu, X., and Squires, K. D., "Generation of inflow data for spatially-developing boundary layer simulations," *J. Comput. Phys.*, Vol. 140, 1998, pp. 233–258.

[29] Bobke, A., Vinuesa, R., Örlü, R., and Schlatter, P., "History effects and near equilibrium in adverse-pressure-gradient turbulent boundary layers," *J. Fluid Mech.*, Vol. 820, 2017, pp. 667–692.

[30] Kitsios, V., Sekimoto, A., Atkinson, C., Sillero, J. A., Borrell, G., Gungor, A. G., Jiménez, J., and Soria, J., "Direct numerical simulation of a self-similar adverse pressure gradient turbulent boundary layer at the verge of separation," *J. Fluid Mech.*, Vol. 829, 2017, pp. 392–419.

[31] Pozuelo, R., Li, Q., Schlatter, P., and Vinuesa, R., "An adverse-pressure-gradient turbulent boundary layer with nearly constant $\beta \simeq 1.4$ up to $Re_\theta \simeq 8700$," *J. Fluid Mech.*, Vol. 939, 2022, p. A34.

[32] Griffin, K. P., Fu, L., and Moin, P., "General method for determining the boundary layer thickness in nonequilibrium flows," *Phys. Ref. Fluids*, Vol. 6, 2021, p. 024608.

[33] Endrikat, S., Modesti, D., MacDonald, M., García-Mayoral, R., Hutchins, N., and Chung, D., "Direct numerical simulations of turbulent flow over various riblet shapes in minimal-span channels," *Flow Turbul. Combust*, Vol. 107, 2021, pp. 1–29.

[34] García-Mayoral, R., and Jiménez, J., "Scaling of turbulent structures in riblet channels up to $Re_\tau \approx 550$," *Phys. Fluids*, Vol. 24, No. 10, 2012, p. 105101.

[35] Endrikat, S., Modesti, D., García-Mayoral, R., Hutchins, N., and Chung, D., "Influence of riblet shapes on the occurrence of Kelvin-Helmholtz rollers," *J. Fluid Mech.*, Vol. 913, 2021, p. A37.

[36] Camobreco, C. J., Endrikat, S., García-Mayoral, R., Luhar, M., and Chung, D., "Why do only some riblets promote spanwise rollers?" *J. Fluid Mech.*, Vol. 1022, 2025, p. A35.

[37] Peskin, C. S., "Flow patterns around heart valves: a numerical method," *J. Comput. Phys.*, Vol. 10, 1972, pp. 552–271.

[38] Scotti, A., "Direct numerical simulation of turbulent channel flows with boundary roughened with virtual sandpaper," *Phys. Fluids*, Vol. 18, No. 3, 2006, p. 031701.

[39] Yuan, J., and Piomelli, U., "Numerical simulations of sink-flow boundary layers over rough surfaces," *Phys. Fluids*, Vol. 26, No. 1, 2014, p. 015113.

[40] Yuan, J., and Piomelli, U., "Roughness effects on the Reynolds stress budgets in near-wall turbulence," *J. Fluid Mech.*, Vol. 760, 2014, p. R1.

[41] Keating, A., Piomelli, U., Bremhorst, K., and Nešić, S., "Large-eddy simulation of heat transfer downstream of a backward-facing step," *J. Turbul.*, Vol. 5, 2004, pp. N20 1–27.

[42] Savino, B. S., and Wu, W., "Thrust generation by shark denticles," *J. Fluid Mech.*, Vol. 1000, 2024, p. A80.

[43] Savino, B. S., and Wu, W., "Impact of spanwise rotation on flow separation and recovery behind a bulge in channel flows," *J. Fluid Mech.*, Vol. 999, 2024, p. A51.

[44] Kim, J., and Moin, P., "Application of a fractional-step method to incompressible Navier-Stokes equations," *J. Comput. Phys.*, Vol. 59, 1985, pp. 303–323.

[45] Moin, P., *Fundamentals of Engineering Numerical Analysis*, Cambridge University Press, 2010.

[46] Raupach, M. R., Antonia, R. A., and Rajagopalan, S., "Rough-wall boundary layers," *App. Mech. Rev.*, Vol. 44, No. 1, 1991, pp. 1–25.

[47] Nikora, V., McEwan, I., McLean, S., , Coleman, S., Pokrajac, D., and Walters, R., "Double-averaging concept for rough-bed open-channel and overland flows: Theoretical background," *J. Hydraul. Eng.*, Vol. 133, No. 8, 2007, pp. 873–883.

[48] Mignot, E., Barthelemy, E., and Hurther, D., "Double-averaging analysis and local flow characterization of near-bed turbulence in gravel-bed channel flows," *J. Fluid Mech.*, Vol. 618, 2009, pp. 279–303.

[49] Wu, W., and Piomelli, U., "Effects of surface roughness on a separating turbulent boundary layer," *J. Fluid Mech.*, Vol. 841, 2018, pp. 552–580.

[50] Gatti, D., von Deyn, L., Forooghi, P., and Frohnapfel, B., "Do riblets exhibit fully rough behaviour?" *Experiments in Fluids*, Vol. 61, No. 3, 2020, p. 81.

[51] Rouhi, A., Endrikat, S., Modesti, D., Sandberg, R. D., Oda, T., Tanimoto, K., Hutchins, N., and Chung, D., "Riblet-generated flow mechanisms that lead to local breaking of the Reynolds analogy," *J. Fluid Mech.*, Vol. 951, 2022, p. A45.

[52] Abu Rowin, W., Deshpande, R., Wang, S., Kozul, M., Chung, D., Sandberg, R. D., and Hutchins, N., "Experimental characterisation of Kelvin-Helmholtz rollers over riblet surfaces," *J. Fluid Mech.*, Vol. 1009, 2025, p. A65.